

Melting of olive oil in immiscible surroundings: experiments and theory

Pim Waasdorp, Aron H. van den Bogaard,
Leen van Wijngaarden, and Sander G. Huisman†

Physics of Fluids Group and Max-Planck Center for Complex Fluid Dynamics, Faculty of Science and Technology, J.M. Burgers Center for Fluid Dynamics, University of Twente
7500 AE Enschede, The Netherlands

(Received xx; revised xx; accepted xx)

We report on the melting dynamics of frozen olive oil in quiescent water for Rayleigh numbers up to 10^9 . The density difference results in an upward buoyancy-driven flow of liquid oil forming a thin film around the frozen oil. We experimentally investigate flat, cylindrical, and spherical shapes and we derive theoretical expressions for the local film thickness, velocity, and the local melt rate for these three canonical geometries. Our theoretical models compare favourably with our experimental findings.

Keywords: Solidification/melting, Buoyant boundary layers

1. Introduction

Understanding the complicated dynamics of phase change is relevant to predict and control many natural and industrial processes. Melting and dissolution are examples of the classical Stefan problem, where the boundary is defined by the phase of the material and the evolution of the boundary follows from the material undergoing phase change. Common examples include the freezing of water to make ice cubes, novel developments in phase change materials, where the latent heat of fusion is used as a temporary energy storage (Dhaidan & Khodadadi 2015), and the melting of ice around Earth’s North and South Poles (Holland *et al.* 2006; Feltham 2008; Cenedese & Straneo 2023).

During melting, the cold melt generally flows along the body, giving rise to non-uniform melting, and therefore changing the shape of the object, which then feeds back on the flow. This shape change or self-sculpting process of objects subject to melting, erosion, or dissolution has been a topic of recent interest. The evolution of eroding clay spheres and cylinders have been studied by Ristroph *et al.* (2012). More recently, more studies have been done with quiescent surroundings, as in Cohen *et al.* (2016); Davies Wykes *et al.* (2018); Pegler & Davies Wykes (2020); Cohen *et al.* (2020), where they studied the pattern formation due to natural convection and dissolution of hard candy and salt, submerged in water. Pattern formation was also studied by Gu erin *et al.* (2020) who, using experiments, reveal the dynamics of karst geomorphology and rillenkarren formations. Further insights into the emergence of rock formations due to dissolution are provided by Davies Wykes *et al.* (2018) and Huang *et al.* (2020), who emphasise the importance of the directionality of the shaping process. Recently there have been direct numerical simulations by Yang *et al.* (2023*a,b*), who use the phase-field method to study the morphology of melting ice in a Rayleigh–B enard geometry and stratification of salt concentration around a melting cylinder.

Hitherto, all studies on melting mentioned have focused on the melting of miscible

† Email address for correspondence: s.g.huisman@utwente.nl

fluids, i.e. a frozen object submerged in the same substance in liquid phase, or a similar miscible liquid or solution (e.g. melting of ice in salty water). The case of immiscible melting has not yet been explored. Immiscible melting can be achieved in two ways: either we have organic compounds like oils and waxes and combine that with water, or we have metals (e.g. gallium) inside water or oils. The most experimentally-accessible option is to use an oil with a freezing point around 0 °C and water around room temperature, and therefore in this work we study the melting process of frozen olive oil in water.

For thermal convection problems with phase-change the three dimensionless control parameters are the Rayleigh ($\text{Ra}_o = \frac{g(\rho_w - \rho_o)L^3}{\nu_o \alpha_o \rho_o}$), Stefan ($\text{Ste} = \frac{c_p \Delta T}{L}$), and Prandtl ($\text{Pr} = \nu_o / \alpha_o$) numbers. Here, the Rayleigh number is the ratio of the time scale associated to thermal transport due to diffusion, as compared to the time scale of thermal transport due to convection. Whereas in classical Rayleigh–Bénard convection buoyancy is created by (generally) small density changes due to temperature changes ($\beta \Delta T$), in our case a large density difference is immediately created due to the different substances ($(\rho_w - \rho_o) / \rho_o$). A high Rayleigh number means intense thermal driving of the system. The Stefan number describes the ratio of specific heat versus the latent heat of fusion, where the latent heat is the heat needed or released by a phase change. A higher Stefan number means that phase change happens faster. The Prandtl number is a material property describing the ratio of the momentum diffusivity to the thermal diffusivity, and determines whether the thermal boundary layer is embedded in the momentum boundary layer or vice versa.

The present work has the following structure: in section 2 we describe the experimental setup. In section 3, results for the melt rate of frozen olive oil are shown for three different geometries: a vertical wall, a cylinder, and a sphere. For the cylinder we show two different initial Rayleigh numbers (initial sizes). The obtained local melt rates are compared with theoretical models that are derived in detail in section 4. The effect of the assumption of constant viscosity is discussed, and a correction for the variation of the viscosity with temperature is derived. Lastly, we discuss our findings in detail in section 5 and finish with our conclusions in section 6.

2. Experimental setup

The schematic in figure 1 shows the experimental setup we use to study the melting of frozen olive oil. We use a rectangular glass tank of 400 mm × 500 mm × 800 mm, filled with water. During the melting process, the water is quiescent and assumed to be at a constant room temperature $T_\infty = 20$ °C. A small PVC holder (poor thermal conductivity) is included in the frozen olive oil during the freezing process and is attached to a support that is submerged in water. The olive oil has a melting point of $T_o = -8$ °C and is cooled down to a temperature of $T_i = -14$ °C. Further material properties of both substances can be found in table 1. We study three different canonical geometries: a vertical wall, a horizontal cylinder, and a sphere, see figure 1. Since $\rho_{\text{oil}} < \rho_{\text{water}}$ the melted olive oil will rise and collect at the top of the object after which it periodically pinches off. The melting process is recorded through interval imaging. For this, a DSLR camera (Nikon D850) with a 100 mm macro objective (Zeiss Makro Planar T* 2/100) is used. An LED light source and light diffuser are used to create a uniformly-lit background. The images are binarized after which we find the contour, area, and, for the cylinders and spheres, the centroid of the object, see figures 2b and 2c. From the evolution of the contour we find the local melt rate.

The image processing is applied to all images that are taken during an experiment, typically with an interval time of $\Delta t = 10$ s. In figure 2c contours from a single experiment

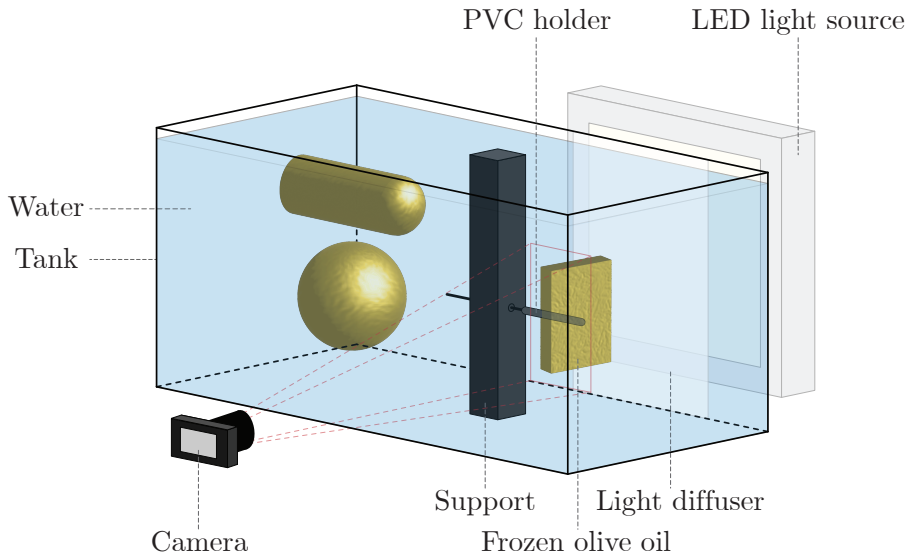


FIGURE 1. Schematic of the experimental setup. The frozen olive oil object is submerged in quiescent water. The dimensions of the glass tank are $400 \text{ mm} \times 500 \text{ mm} \times 800 \text{ mm}$. A PVC holder is incorporated in the frozen oil during freezing, and connects the frozen oil to a support. A white LED light source is used with a light diffuser to create a uniform background illumination. Three canonical geometries are shown: vertical wall (photographed), horizontal cylinder, and sphere. A camera periodically photographs the melting objects from the side (vertical wall) or the front (cylinder and sphere).

	T_m [$^{\circ}\text{C}$]	ρ [kg/m^3]	μ [$\text{kg}/(\text{m} \cdot \text{s})$]	α [mm^2/s]	λ [$\text{W}/(\text{K} \cdot \text{m})$]	c_p [$\text{J}/(\text{kg} \cdot \text{K})$]	\mathcal{L} [kJ/kg]
Water	0	999.65	$1.308 \cdot 10^{-3}$	0.138	0.579	4180	334
Olive oil	-8	860	$170 \cdot 10^{-3}$	0.080	0.170	1970	267

TABLE 1. Material properties of water and olive oil. Properties for water are taken at $T = 10^{\circ}\text{C}$, following Bejan (1993). Thermal properties for olive oil are taken from Carbajal Valdez *et al.* (2006); Turgut *et al.* (2009). Values are taken for a constant temperature of 3°C ; the mean temperature in the olive oil melt layer. The value for the latent heat of fusion is taken from EasyCalculation.com (2005). Comparing with values for other vegetable oils from Gudheim (1944) we find that they are of comparable magnitude.

are shown at different times. Such an image shows a qualitative description of the melting process of the sphere. The contours at the top are more closely spaced, whereas contours at the bottom are more distant, revealing that the melt rate at the bottom of the sphere is higher than the melt rate at the top.

3. Results

Here we will look at the melt rates obtained from the experiments. We will then compare these to analytical expressions—derived in the next section—and discuss the

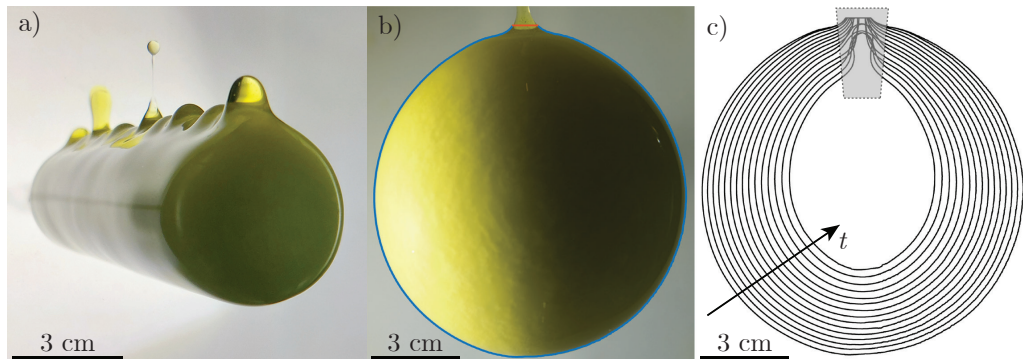


FIGURE 2. a) Melting of a horizontal cylinder in ambient water showing several stages of the droplet pinch-off at the top where the melted olive oil collects. b) Example image from a melting sphere experiment with the contour that is obtained from image analysis overlaid on the original image. Note that the region where the liquid olive oil melt collects and periodically pinches off from the sphere is ignored. c) Contours of a melting sphere for $t = 200$ s to 3200 s, with intervals of 200 s. Note that the tracking on the top side of the sphere is hindered by the collecting and periodically pinching-off of liquid olive oil melt. Therefore, data is ignored in the grey shaded region.

applicability of the theory for the vertical wall, for the two horizontal cylinders, and lastly for a sphere.

3.1. Vertical wall

We first look at the case of the melting of a block of olive oil of 30 cm height. We calculate the horizontal local melting rate from the evolving contours, see figure 3. The profiles in the early stages of the melting process, where the shape, despite slightly changing over time, can be regarded as vertical. At later times, the profile of the initially rectangular block has sculpted itself away from its rectangular shape. While the total process of melting takes about 40 min, here we just show melt rates obtained during the first 5 min. In the lower regions of the vertical wall ($z < 2$ cm), the effects of the finite size of the object can be felt (the bottom corner is rounded over time). We do not show the upper edge region of the melting wall, since the results are heavily influenced by the accumulation and detaching of oil droplets. Away from the top and bottom corners it can be seen that the melt rates are remarkably constant over time, in both scaling ($U \propto z^{-1/4}$) and magnitude. The grey dotted line shows the theoretical model with constant viscosity in the melt layer, whereas the black dashed line shows the theoretical model where the viscosity $\mu(T)$ varies in the melt layer (see section 4.1). We find that our analytical expression predicts our measured data satisfactory in this region. Note that our model does not contain any fitting parameters, and even though several assumptions have been made, there is agreement between the model and the experiments. It is clear that inclusion of variable viscosity is paramount in order to predict the correct melting rate. Henceforth, we only show models with temperature-dependent variable viscosity in the melting layer.

3.2. Cylinder

We perform experiments for horizontal cylinders with initial radii 25 mm and 60 mm corresponding to Rayleigh numbers $Ra \approx 10^7$ and $Ra \approx 10^8$. Figure 4 shows the radial melt rates $U(\theta) = dr(\theta)/dt$ for the small and large cylinder, as a function of the polar angle θ , where $\theta = 0^\circ$ is at the bottom of the cylinder. The theoretical model, without

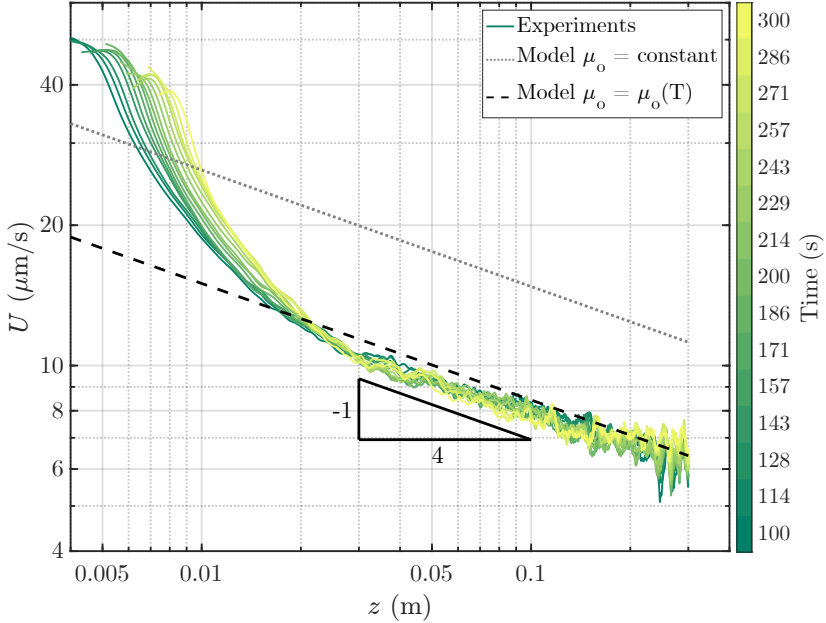


FIGURE 3. Horizontal melt-rate as a function of the height of the vertical wall for $Ra = \mathcal{O}(10^9)$. We show two theoretical approximations, that are derived in a later section. Here the theoretical approximation with constant viscosity μ_o is shown in the grey dotted line, and an approximation with μ_o varying with temperature, and over the thickness of the melt layer, is shown in the black dashed line. The intermediate part of the profile shows a scaling of $-1/4$ with the height. Profiles for times from 100 s until 300 s from the start of the melting process are shown. At later times the vertical wall is no longer an appropriate approximation.

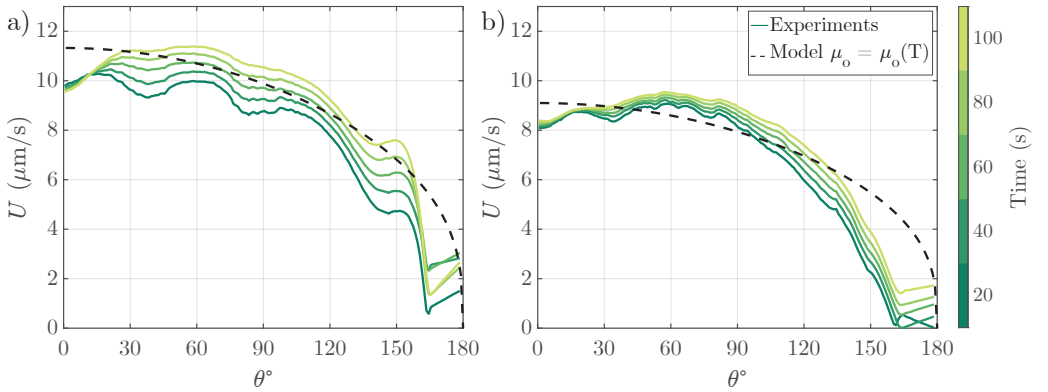


FIGURE 4. a) Cross-sectional melt-rate as a function of the angle θ (polar angle starting from the bottom, see figure 9) for a small cylinder ($R_0 = 25$ mm) $Ra = \mathcal{O}(10^7)$. The black dashed line shows the theoretical model for the cylindrical geometry. b) Large cylinder ($R_0 = 60$ mm) $Ra = \mathcal{O}(10^8)$.

any fitting parameter, for the cylindrical geometry is included as a black dashed line. Here the temperature-dependent viscosity is included in our model. We, again, show the melt rate only for early stages of the melting process, as only for relatively short times the shape can be regarded as cylindrical—as assumed by the model. A reasonable agreement is found between our experiments and our model for both cylinders in a range of angles from $60^\circ \leq \theta \leq 150^\circ$. There are some notable differences between the model and the

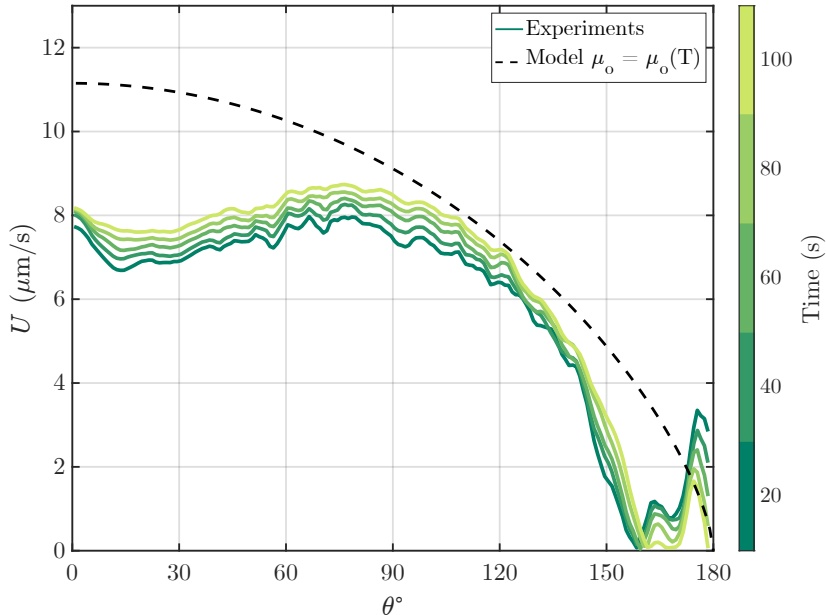


FIGURE 5. Cross-sectional inward melt-rate of a sphere as a function of the angle θ for $Ra = \mathcal{O}(10^8)$. Note that $\theta = 0^\circ$ is at the bottom of the sphere. The solid green lines are results from the experiments. The black dashed line is the theoretical model for the spherical geometry. Note that now we only show the model with temperature-dependent viscosity.

experimental observations, more than for the vertical wall. The melting process of the cylindrical shape has a maximum melt rate along the surface at an angle of $\theta \approx 60^\circ$ from the bottom, whereas the theory predicts a monotonic decrease with increasing θ , such that the predicted maximum melt rate is at the bottom. For $\theta \geq 160^\circ$ the theory and experiments do not match due to the collection of melt at the top before pinching off (Shi *et al.* 1994) at the top of the cylinder and rising to the water surface. The small cylinder has a higher melt rate than the large cylinder, which we can precisely predict from our theory since $U \propto R^{-1/4}$ (equation 4.41) gives us a ratio of 1.24 in the melt rates which we also see in our experiments.

3.3. Sphere

Finally we look at the melting of a sphere with initial radius $R = 60$ mm, see figure 2b. Figure 5 shows the melt rate for this sphere and compares the experiments with the theory. Note that we also included temperature-dependent viscosity in our model. Like for the cylinders, compared to the vertical wall there is more deviation between theory and experiments, but again around $75^\circ \leq \theta \leq 135^\circ$, the model shows reasonable agreement. Deviations for $\theta \leq 75^\circ$ may be caused by the ambient water which we will discuss in section 5. For high angles ($\theta \geq 160^\circ$) the oil layer is much thicker and the flow is influenced by periodically-detaching droplets.

4. Theory

In this section we will derive the analytical models for the melt rate of the frozen olive oil objects that were shown in figures 3, 4, and 5. We start with the theory for the vertical wall. After deriving this model we realized, from comparison with the experimental results, that it was needed to include temperature-dependent viscosity, and

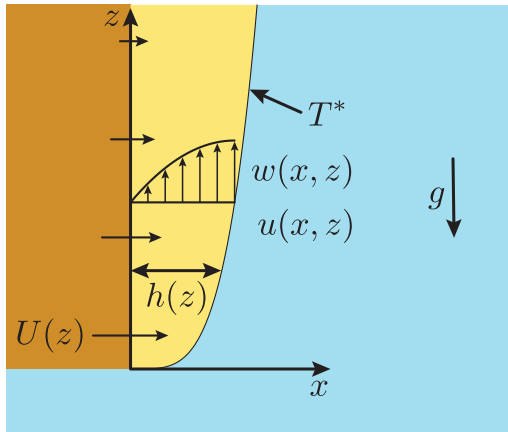


FIGURE 6. Schematic overview of melted olive oil (yellow) at a flat plate of frozen olive oil (orange), submerged in water. $U(z)$ is the melt rate at the frozen/liquid oil interface.

we incorporate this in the analysis. Using this as a starting point we then derive the theory for the cylindrical geometry and the spherical geometry.

Vertical wall

We start with the melting of the vertical wall, as shown in figure 6. With horizontal and vertical axes x and z , respectively, the frozen wall is along the z -axis at $x = 0$, the liquid melt layer is between $0 \leq x \leq h(z)$ while the ambient water, causing the oil to melt, stretches from $x = h(z)$ to infinity in x -direction. The surrounding water is cooling down as the oil is melting and therefore flows downward under the influence of gravity, reaching velocities in the order of cm/s. These velocities are relatively low and as such we will assume that the ambient water is stationary. Inside the melt layer we have the horizontal velocity u and the vertical velocity w in the x and z directions, respectively. Gravity has acceleration g in the negative z direction. The properties of the oil are labeled with the subscript o and those of water with w . The most important are the densities ρ_o and ρ_w and the dynamic viscosities μ_o and μ_w . Under these circumstances, where the oil is very viscous, and assuming we are in a steady state, the w -component of the Navier–Stokes equations simplifies such that we have a balance between the pressure gradient due to buoyancy and the viscous forces:

$$\mu_o \left(\frac{\partial^2 w}{\partial x^2} + \frac{\partial^2 w}{\partial z^2} \right) - g(\rho_o - \rho_w) = 0. \quad (4.1)$$

At the interface between solid and liquid oil we have $w(x = 0) = 0$. The film has a thickness of $\mathcal{O}(\text{mm})$, very small with respect to the height (30 cm), such that we are in the thin film limit ($\frac{\partial}{\partial x} \gg \frac{\partial}{\partial z}$) and we can therefore neglect the derivatives in the z -direction in equation 4.1. In addition, the viscosity of the olive oil is much larger than that of water (table 1), such that the velocity gradient at the water-oil interface $\frac{\partial w}{\partial x} \Big|_{x=h(z)} \approx 0$. The solution of a simplified equation 4.1 and obeying these boundary conditions then is:

$$w(x, z) = \beta x(2h(z) - x) \quad \text{with: } \beta = \frac{g(\rho_w - \rho_o)}{2\mu_o} = \frac{g\Delta\rho}{2\mu_o}. \quad (4.2)$$

From the continuity equation follows the horizontal velocity:

$$\frac{\partial u}{\partial x} = -\frac{\partial w}{\partial z} = -2\beta x \frac{dh}{dz}. \quad (4.3)$$

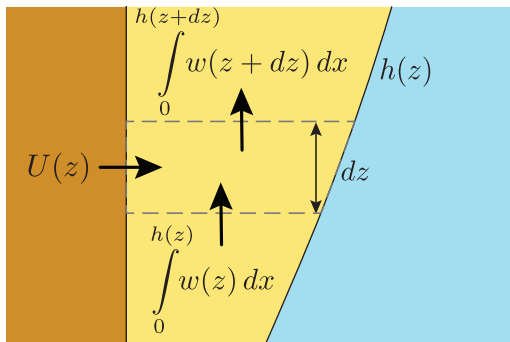


FIGURE 7. Illustration of the mass flows in a small control volume (dashed grey) of melting olive oil at a vertical wall. Oil is ‘injected’ into the volume from the wall since the left of the control volume is following the interface, and oil enters the volume from below due to buoyancy forces. The total ingress from these two contributions equals the egress at the top of the control volume.

We can now find the melt rate $U(z)$ at which the wall melts by integrating the previous equation to obtain:

$$u(x, z) = U(z) - \beta x^2 \frac{dh}{dz}. \quad (4.4)$$

From mass conservation, see figure 7, we can relate the melt rate and the film thickness:

$$U(z) = \frac{\partial}{\partial z} \left(\int_0^h w dx \right) = \frac{\partial}{\partial z} \left(\frac{2}{3} \beta h(z)^3 \right). \quad (4.5)$$

To find $h(z)$ we need to consider the thermal transport. The ambient water, with a temperature of 20 °C far away, transfers heat to the melt layer. This, in turn, transfers heat to the solid oil, causing this to melt further. We first consider the advection-conduction equation inside the thin melt layer. Assuming stationarity and using the thin film approximation we arrive at a balance between convection and diffusion:

$$u \frac{\partial T}{\partial x} = \alpha \frac{\partial^2 T}{\partial x^2}, \quad (4.6)$$

where $\alpha = (\lambda/\rho c_p)_o$ is the thermal diffusivity, λ is the thermal conductivity, and c_p is the specific heat capacity. One boundary condition is that T equals the melting temperature T_o at $x = 0$. At the interface of the melt layer and the ambient water, $x = h$, temperature and heat flux must be continuous. Since the velocity is small in both the oil and water, heat conduction is prominent. At the boundary, the water flowing down is only in contact with the wall for a short time. Therefore, we approximate here the temperature at the interface between water and oil with the so-called contact temperature, occurring when two semi-infinite media with different temperature are brought in contact. With material properties $f = \sqrt{\lambda \rho c_p}$, this contact temperature is then (see e.g. section 5.7, equation (5.63) from Incropera & Witt (1990)):

$$T^* = \frac{f_o T_o + f_w T_\infty}{f_o + f_w}, \quad (4.7)$$

where T_∞ is the temperature of the water far away. Filling in the values for water and oil we get:

$$T^* = T_o + 0.74(T_\infty - T_o).$$

The solution of equation 4.6 with T_o at $x = 0$ and $T = T^*$ at $x = h$ results in

$$T(x, z) = T_o + 0.74(T_\infty - T_o) \frac{\int_0^x e^{\frac{U(z)x}{\alpha} - \frac{\beta x^3 \frac{d}{dz} h(z)}{3\alpha}} dx}{\int_0^h e^{\frac{U(z)x}{\alpha} - \frac{\beta x^3 \frac{d}{dz} h(z)}{3\alpha}} dx} \quad (4.8)$$

The heat flux at the wall, $\lambda(dT/dx)_{x=0}$, results in the melting rate. With latent heat \mathcal{L} this means that

$$\lambda(dT/dx)_{x=0} = U(z)\rho_o\mathcal{L}. \quad (4.9)$$

Combining equations 4.4 and 4.8 gives:

$$\beta \frac{d}{dz} (h^4) \int_0^1 e^{\frac{\beta \frac{d}{dz} (h^4) \xi}{2\alpha} - \frac{\beta \frac{d}{dz} (h^4) \xi^3}{12\alpha}} d\xi = \frac{2 \cdot 0.74\lambda(T_\infty - T_o)}{\rho_o\mathcal{L}}, \quad (4.10)$$

where $\xi = x/h$. The integral in equation 4.10 cannot be written as an analytic expression. In order to evaluate the integral we approximate the integrand by only taking the first term in the argument of the exponent, which means that in equation 4.4 we only take the first term. We then find:

$$h(z) = z^{1/4} \left[\frac{2\alpha}{\beta} \ln(1 + \Lambda) \right]^{1/4}, \quad (4.11)$$

$$\Lambda = 0.74(T_\infty - T_o) \frac{c_p}{\mathcal{L}} = 0.74\text{Ste}. \quad (4.12)$$

For comparison with experiments, $U(z)$ is the best quantity. From equations 4.5 and 4.11 we have:

$$U(z) = \frac{\alpha}{h} \ln(1 + \Lambda) \propto z^{-1/4}, \quad (4.13)$$

which scales with the height z to a power of $-1/4$. This exponent been shown before in similar configurations by Wagner (1949); Ostrach (1953); Merk & Prins (1954); Wells & Worster (2011). The predicted melt rate in equation 4.13 is drawn in figure 3 as the grey dotted line. This shows that the slope agrees satisfactory with the experimental data, but the values are considerably higher. So far we had approximated the viscosity of the oil to be constant inside the melt layer, however, the strong temperature gradient inside the melt layer does not allow us to model the viscosity as constant. The temperature dependence of the viscosity of the oil is shown in figure 8 for the relevant temperature range. The temperature at the wall is -8°C and the temperature at the oil-water interface is $T^* = 13^\circ\text{C}$. The viscosity varies from 400 cP to 100 cP over this interval. In the following section we calculate again the vertical velocity w in the melt, however, now taking a variable viscosity into account.

4.1. Variation in viscosity

In table 1 we state a value for the viscosity of olive oil of 170 cP. This value is taken at a mean olive oil temperature of 3°C . An Anton Paar MCR502 rheometer was used to measure temperature dependence of the viscosity of the olive oil, see figure 8. As the oil is cooling down and approaching its freezing temperature its viscosity is increasing substantially. To account for the variation in the viscosity, we recalculate the vertical

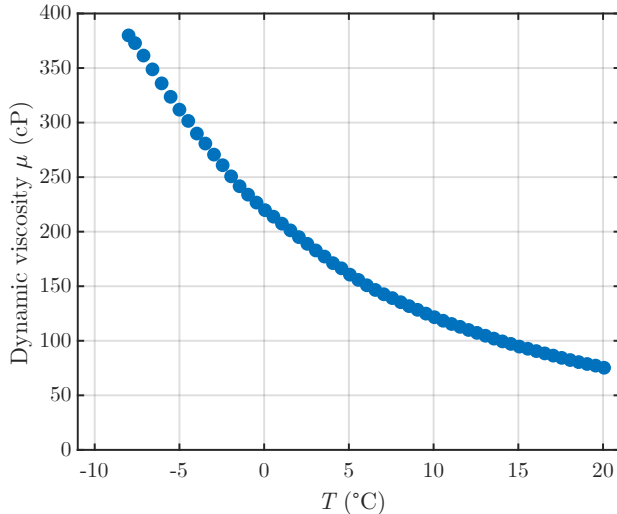


FIGURE 8. Olive oil viscosity as a function of the temperature. Measurements are done using an Anton Paar MCR502 rheometer with Peltier cooling. Measurements are done starting at a temperature of 20 °C and decreasing step-wise to a minimum of -8 °C.

velocity w . We assume a linear profile for viscosity between the two boundary values:

$$\mu_o(x) = \mu_o(T_o) \left(1 - \frac{x}{h}\right) + \mu_o(T^*) \frac{x}{h}. \quad (4.14)$$

The equation for the vertical velocity (equation 4.1) is now modified (which is different from the standard form of the Navier–Stokes equations where constant viscosity is assumed):

$$\frac{\partial}{\partial x} \left(\mu_o(x) \frac{\partial w}{\partial x} \right) = -g\Delta\rho. \quad (4.15)$$

After integrating once we obtain:

$$\left(\left(1 - \frac{x}{h}\right) \mu_o(T_o) + \frac{x}{h} \mu_o(T^*) \right) \frac{\partial w}{\partial x} = -g\Delta\rho x + C. \quad (4.16)$$

The boundary conditions remain unchanged:

$$w|_{x=0} = 0, \quad (4.17)$$

$$\left. \frac{\partial w}{\partial x} \right|_{x=h} = 0. \quad (4.18)$$

We find the integration constant C from using the boundary equation 4.18:

$$\frac{\partial w}{\partial x} = \frac{g\Delta\rho(h-x)}{\left(1 - \frac{x}{h}\right) \mu_o(T_o) + \frac{x}{h} \mu_o(T^*)}. \quad (4.19)$$

We introduce the dimensionless quantity $\tilde{\mu}$:

$$\tilde{\mu} = \frac{\mu_o(T^*) - \mu_o(T_o)}{\mu_o(T_o)}. \quad (4.20)$$

Using this definition, equation 4.19 can be rewritten and we obtain:

$$\frac{\partial w}{\partial x} = \frac{2\beta h(h-x)}{h + \tilde{\mu}x}. \quad (4.21)$$

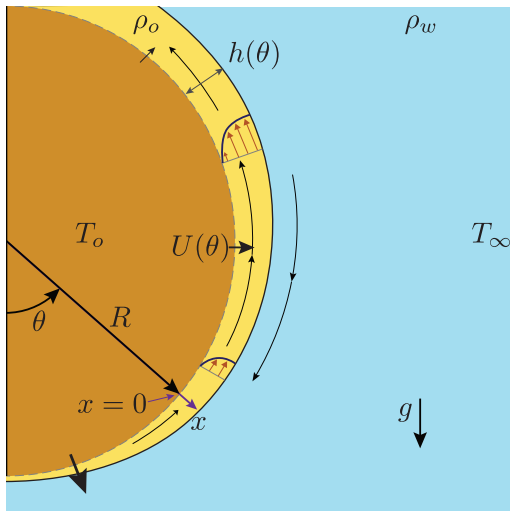


FIGURE 9. Schematic overview of molten olive oil (yellow) over a circular shape of frozen olive oil (orange), submerged in water (blue). $U(\theta)$ is the melt rate at the frozen/liquid oil interface.

After integrating and applying the boundary condition 4.17 we get:

$$w(x, z) = 2\beta h^2 \left(\frac{\tilde{\mu} + 1}{\tilde{\mu}^2} \ln \left(\frac{\tilde{\mu}x}{h} + 1 \right) - \frac{x}{h\tilde{\mu}} \right). \quad (4.22)$$

We see by expansion in $\tilde{\mu}$ that for $\tilde{\mu} = 0$, w is the same as in equation 4.2. Note that w is still a function of both x and z , since h is a function of the height. As before, to get the melt rate $U(z)$ we integrate over a control volume in the liquid melt layer (see equation 4.5).

$$U(z) = \frac{d}{dz} \left(\beta \frac{2}{3} h(z)^3 \right) \left(\frac{3(1 + \tilde{\mu})^2}{\tilde{\mu}^3} \ln(1 + \tilde{\mu}) - \frac{6 + 9\tilde{\mu}}{2\tilde{\mu}^2} \right). \quad (4.23)$$

Comparing this result with the previously found expression for melt rate $U(z)$ (r.h.s. of equation 4.5), it is seen that the varying viscosity introduces a correction on the melt rate that is dependent on the values for the viscosity at the wall and at the oil-water interface.

Cylinder

For the horizontal cylinder (see figure 2a), we need to perform a coordinate transform to polar coordinates, see figure 9. The buoyancy term β now depends on the angle θ with the vertical direction, and the coordinate transform is applied to the governing equations. The melt rate U and film thickness h now depend on the angle θ instead of height z . Since $h \ll R$ with R the radius of the cylinder, the tangential velocity (with $x = r - R$) has the same profile as w for the vertical wall. Equation 4.24 shows the continuity equation in polar coordinates where the axial dependence has been assumed absent, where u_r is the radial velocity, and u_θ is the tangential velocity, with $u_\theta = \beta x(2h(\theta) - x)$ analogous to the vertical velocity w for the vertical wall. $\tilde{\beta} = \beta \sin \theta$ is the buoyancy term adapted to the geometry.

$$\frac{\partial}{\partial x} ((R + x)u_r) = \frac{\partial}{\partial \theta} (u_\theta). \quad (4.24)$$

Substituting u_θ in equation 4.24 and using an analogous boundary condition to the vertical wall case, $u_r(x=0) = U(\theta)$, results in an expression for u_r :

$$u_r(\theta, x) = U(\theta) + \frac{1}{R} \left(-\frac{1}{3} \frac{d}{d\theta} (\bar{\beta}) x^3 + \frac{d}{d\theta} (\bar{\beta} h) x^2 \right). \quad (4.25)$$

An expression for the melt rate can be obtained by considering mass conservation:

$$U(\theta) = \frac{1}{R} \frac{\partial}{\partial \theta} \int_0^{h(\theta)} u_\theta(\theta, x) dx = \frac{1}{R} \frac{d}{d\theta} \left(\frac{2}{3} \bar{\beta} h^3 \right). \quad (4.26)$$

The advection-conduction equation, analogous to equation 4.6, with $\xi = \frac{x}{h}$, follows:

$$u_r \frac{\partial T}{\partial \xi} = \frac{\alpha}{h} \frac{\partial^2 T}{\partial \xi^2}. \quad (4.27)$$

The boundary conditions are analogous to the case of a vertical wall:

$$T|_{\xi=0} = T_o, \quad (4.28)$$

$$T|_{\xi=1} = T_o + 0.74\Delta T. \quad (4.29)$$

The solution for the temperature profile is:

$$T(\xi) = T_o + 0.74\Delta T \frac{\int_0^\xi \exp \left[\frac{2h}{3R\alpha} \frac{d}{d\theta} (\bar{\beta} h^3) \xi \right] d\xi}{\int_0^1 \exp \left[\frac{2h}{3R\alpha} \frac{d}{d\theta} (\bar{\beta} h^3) \xi \right] d\xi}. \quad (4.30)$$

Analogous to equation 4.9 the heat flux balance is:

$$\rho_o U(\theta) \mathcal{L} = \frac{0.74\Delta T \lambda}{h} \frac{1}{\int_0^1 \exp \left[\frac{2\beta h}{3R\alpha} \frac{d}{d\theta} (\sin(\theta) h^3) \xi \right] d\xi}. \quad (4.31)$$

We define the quantities

$$q^4 = \frac{R\alpha}{\beta}, \quad \text{and} \quad H = \frac{h^4}{q^4}. \quad (4.32)$$

Then the integral in equation 4.31 becomes

$$\int_0^1 \exp \left[\left(\frac{1}{2} \frac{dH}{d\theta} \sin(\theta) + \frac{2}{3} H \cos(\theta) \right) \xi \right] d\xi. \quad (4.33)$$

We define a function $G(\theta)$:

$$G(\theta) = \frac{2}{3} H \cos(\theta) + \frac{1}{2} \frac{dH}{d\theta} \sin(\theta). \quad (4.34)$$

Such that we can write the integral as:

$$\int_0^1 \exp [G(\theta)\xi] d\xi. \quad (4.35)$$

From equations 4.26, 4.32, and 4.34 we deduce that

$$hU(\theta) = \alpha G(\theta). \quad (4.36)$$

Inserting this into equation 4.31 and using equation 4.35 results in

$$\frac{0.74}{\alpha} = \exp(G(\theta)) - 1. \quad (4.37)$$

With equation 4.13 and taking logarithms we arrive at:

$$G(\theta) = \frac{2}{3}H \cos(\theta) + \frac{1}{2} \frac{dH}{d\theta} \sin(\theta) = \ln(1 + \Lambda). \quad (4.38)$$

Solving and requesting regularity at $\theta = 0$ gives:

$$H = \left(\frac{h}{q}\right)^4 = 4 \ln(1 + \Lambda) \frac{\int_0^\theta \sin(\theta^*)^{1/3} d\theta^*}{\sin(\theta)^{4/3}}. \quad (4.39)$$

The final solution for the melt film thickness and melt rate can now be found by rewriting equation 4.39, using equation 4.32, and substituting the result for the melt film thickness in equation 4.36:

$$h_{\text{cyl}}(\theta) = R^{1/4} \left[\frac{2\alpha}{\beta} \ln(1 + \Lambda) \right]^{1/4} f_{\text{cyl}}(\theta), \quad (4.40)$$

$$U_{\text{cyl}}(\theta) = \frac{\alpha}{h_{\text{cyl}}} \ln(1 + \Lambda). \quad (4.41)$$

where $f_{\text{cyl}}(\theta)$ is a shape function:

$$f_{\text{cyl}} = \frac{\left(\int_0^\theta \sin(\theta^*)^{1/3} d\theta^* \right)^{1/4}}{\sin(\theta)^{1/3}}, \quad (4.42)$$

$$= \begin{cases} \frac{\sqrt[4]{3} {}_2F_1\left(\frac{1}{2}, \frac{2}{3}; \frac{5}{3}; \sin(\theta)^2\right)}{\sqrt{2}} & 0 \leq \theta \leq \frac{\pi}{2} \\ \frac{\sqrt[4]{\frac{3\sqrt{3}\Gamma\left(\frac{2}{3}\right)^3}{2^{2/3}\pi} - \frac{3}{4} \sin(\theta)^{\frac{4}{3}} {}_2F_1\left(\frac{1}{2}, \frac{2}{3}; \frac{5}{3}; \sin(\theta)^2\right)}}{\sqrt[3]{\sin(\theta)}} & \frac{\pi}{2} \leq \theta \leq \pi \end{cases}, \quad (4.43)$$

where ${}_2F_1$ is Gauss's hypergeometric function and Γ the complete gamma function. Compared to the expressions that were found for the vertical wall, the difference is in this shape function, which compensates for the geometry varying when following the boundary of the wall, and the dependence on the radius $h_{\text{cyl}} \propto R^{1/4}$. Similar expressions occur in Acrivos (1960*a,b*) and also resemble the solutions for a dissolving *vertical* cylinder found by Pegler & Davies Wykes (2020).

Sphere

The problem of a melting sphere is very similar to the cylinder described above. $\theta = 0$ is again defined on the bottom side of the object, the azimuthal angle ϕ is defined positive in clockwise direction, and $x = r - R$, with $x = 0$ at the surface, is defined in the same manner as the horizontal cylinder, see figure 9. An important difference is a flow focusing due to the varying circumference of the sphere with changing polar angle θ . The continuity equation in spherical coordinates, where $u_\theta = \bar{\beta}x(2h - x)$, is unchanged and azimuthal symmetry is assumed:

$$\frac{1}{r^2} \frac{\partial}{\partial r}(r^2 u_r) + \frac{1}{r \sin(\theta)} \frac{\partial}{\partial \theta}(u_\theta \sin(\theta)) = 0. \quad (4.44)$$

From this, u_r can be found as before:

$$u_r = U(\theta) - (2\beta h \cos(\theta) + \beta \frac{dh}{d\theta} \sin(\theta)) \frac{x^2}{R} + \frac{2}{3} \beta \cos(\theta) \frac{x^3}{R}. \quad (4.45)$$

The control volume over the film thickness is now taken in three dimensions:

$$2\pi R^2 \sin(\theta)U(\theta) = \frac{d}{d\theta} \int_0^h 2\pi R \sin(\theta)u_\theta dx, \quad (4.46)$$

which after substitution of u_θ gives:

$$U(\theta) = \frac{1}{R \sin(\theta)} \frac{\partial}{\partial \theta} \left(\frac{2}{3} \beta h^3 \sin(\theta)^2 \right). \quad (4.47)$$

Following a similar procedure as before, we find a new function $G(\theta)$:

$$G(\theta) = \frac{4}{3} \cos(\theta)H + \frac{1}{2} \sin(\theta) \frac{dH}{d\theta} = \ln(1 + \Lambda). \quad (4.48)$$

This can be solved to obtain the final solutions for the film thickness and the melt rate:

$$h_{\text{sphere}}(\theta) = R^{1/4} \left[\frac{2\alpha}{\beta} \ln(1 + \Lambda) \right]^{1/4} f_{\text{sphere}}, \quad (4.49)$$

$$U_{\text{sphere}}(\theta) = \ln(1 + \Lambda) \frac{\alpha}{h_{\text{sphere}}}, \quad (4.50)$$

where f_{sphere} is a shape function for the spherical geometry, different from the one for the cylinder:

$$f_{\text{sphere}} = \frac{\left(\int_0^\theta \sin(\theta^*)^{5/3} d\theta^* \right)^{1/4}}{\sin(\theta)^{2/3}}, \quad (4.51)$$

$$= \begin{cases} \frac{\sqrt[4]{3} {}_2F_1\left(\frac{1}{2}, \frac{4}{3}; \frac{7}{3}; \sin(\theta)^2\right)}{2^{3/4}} & 0 \leq \theta \leq \frac{\pi}{2} \\ \frac{\sqrt[4]{\frac{\sqrt{3}\Gamma\left(\frac{1}{3}\right)^3}{5\sqrt[3]{2}\pi} - \frac{3}{8} \sin(\theta)^{\frac{8}{3}} {}_2F_1\left(\frac{1}{2}, \frac{4}{3}; \frac{7}{3}; \sin(\theta)^2\right)}}{\sin(\theta)^{\frac{2}{3}}} & \frac{\pi}{2} \leq \theta \leq \pi \end{cases}. \quad (4.52)$$

We like to highlight that the solutions for the thickness h (equations 4.11, 4.40, and 4.49) and for the melt rate U (equations 4.13, 4.41, and 4.50) for all three geometries have a very similar form.

5. Discussion

We have shown that our models match relatively well with our experimental findings, especially considering that our model does not contain any free (fitting) parameters. During the derivation we made several approximations, and the model does not include all effects. We will now go through the various approximations and assess their validity.

First, we have made use of the thin film approximation, which seems like a reasonable approximation since our layer thickness is of $\mathcal{O}(\text{mm})$ while our objects are of $\mathcal{O}(100 \text{ mm})$.

Second, we had made the assumption that $\frac{\partial w}{\partial x} \Big|_{x=h} \approx 0$ which also seems justified since the ratio of the viscosities, even in the worst case, is $\mu_o/\mu_w \approx 75 \gg 1$.

Third, in equation 4.10 we had neglected the second term in the exponent. To verify, we can plug in the solution for $h(z)$ (equation 4.11) into the integral and evaluate it numerically. We find that the value of the integral is only 0.6% lower when the cubic term is included as compared to when the term is neglected. We therefore think this approximation is reasonably justified.

Fourth, the assumption of a constant contact temperature T^* along the wall, turns out to be realistic for the vertical wall, and for the cylinder, as can be seen from figures 3 and 4. In the case of the sphere the agreement with the model is good between 60° and 130° but there is a significant difference in the bottom region, see figure 5. The reason for that becomes clear from the following analysis. When two semi-infinite media of different temperatures are brought in contact the interface assumes a temperature, the contact temperature T^* , given in equation 4.7, which remains constant thereafter. In our case one of the media, the melt film, is of finite extent h . If we take, for convenience, equal material properties at both sides, the contact temperature changes in time according to (see Appendix A)

$$T^* = T_o + \frac{T_\infty - T_o}{2} \operatorname{erf} \left(\frac{h}{\sqrt{\alpha t}} \right), \quad (5.1)$$

where $\operatorname{erf}(\tau) = \frac{2}{\sqrt{\pi}} \int_0^\tau e^{-t^2} dt$ is the error function. Given a typical time of 20 s of contact of a water element from top to bottom of the sphere, and a $h = 2 \text{ mm}$, with $\alpha = 8 \cdot 10^{-8}$, this means that after 20 s the error function in equation 5.1 has still 96% of its initial value. However, near the bottom, where $\theta = 0$ and h is very small, of the order of tenths of millimeters, and where probably the contact time is longer, the error function decreases from its initial value. This means a drop in the contact temperature and thereby of the melting rate. For the vertical wall the film thickness is of the order of a 1 mm along most of the wall. Unfortunately we are unable to locally measure the temperature profiles since the scales are too small (and probes too big).

Fifth, we now assumed a linear dependence of the viscosity with x inside the melt layer ($0 \leq x \leq h$). In reality, assuming a linear temperature profile inside the melt layer, we systematically over-predict the viscosity in the middle of the melt layer. So we think that by including a more elaborate viscosity curve, as seen in figure 8, the melting will go, following equation 4.13, slightly faster.

Sixth, throughout the analysis we had assumed that the problem is time-independent. Since our freezing temperature is $T_i = -14 \text{ }^\circ\text{C}$ and the melting point it $T_o = -8 \text{ }^\circ\text{C}$ all the matter has to warm up 6 K before it melts. At $t = 0$ a skin layer of the temperature grows inside the material. The typical dimensionless similarity variable $\eta = x/\sqrt{\alpha t}$ can then be used to find the temperature profile inside the material which goes like $\operatorname{erf}(\eta/2)$. The typical penetration depth of the temperature is thus given by $\sqrt{\alpha t}$, such that the speed at which this front moves is $U_{\text{skin layer}} = \sqrt{\frac{\alpha}{4t}}$. If we equate this to our melt speed of $U \approx 10 \text{ } \mu\text{m/s}$ we find a typical time scale of $t \approx 200 \text{ s}$ at which the speed of the

penetrating skin layer reaches the same speed as the melting boundary. In other words, for times below a few minutes, there is energy spend on heating up material that is not melted in this time. For larger times, the speed of skin layer and the melting boundary moving along at the same speed, and energy is only spent on heating the material that is also melted. This thus means that for small times we overpredict the melting rate, and the actual melting rate is slightly less since we heat more material up than we melt. Note that the energy spent on heating is relatively small as compared to the energy spent on the phase transition $c_p(T_i - T_o)/\mathcal{L} = 4.4\%$, such that the effect is comparatively small. Another experimental issue not yet discussed in detail, might be that, as we remove the frozen oil from the metallic mould and then place in our water tank the oil has slightly heated up. We are not sure whether all objects were -14°C throughout. Whereas the melting profiles U are more or less constant for the vertical wall and the large horizontal cylinder, for the sphere and the small cylinder the melting profiles U change a bit over time. The reason between those could be the varying time between releasing the olive oil from the mould and placing them in our aquarium, see figure 1. We hypothesize that for the vertical wall and the large cylinder the object was left (relatively) long in air and would already start forming the temperature skin layer. For the experiments with the small cylinder and the sphere we quickly used the sphere after releasing it from the mold, not allowing the temperature skin layer to develop. This could then explain the differences in steadiness between the melting profiles U for the various geometries.

Lastly, throughout our derivation we have considered the ambient water to be stationary. We suspect that the influence of the water is small but not negligible. The cold melted olive oil will cool down the water, giving rise to a cold downward flow, resulting in two stacked boundary layers—flowing in opposite directions. This will therefore locally influence the contact temperature T^* . The velocity in the oil layer is of order 1 mm/s and the velocity in water 1 cm/s. This is so low that heat transfer is still mainly by conduction and will influence T^* in a small amount.

6. Conclusion

In this work we have studied the melting process of frozen olive oil in an immiscible environment of water. We have studied three different geometries with different symmetries experimentally and model the melt rate along the interface. Our model can predict the height (or angular) dependence of the melt rate for the three geometries, and not only the scaling but also the prefactor can be predicted such that our model is without fitting parameters. For the vertical wall our model matches well with the experiments. For the cylindrical and spherical geometries the agreement is less good but still showing the approximate profile and the right order of magnitude.

7. Acknowledgements

We thank Gert-Wim Bruggert, Dennis van Gils, Martin Bos, and Thomas Zijlstra for technical support. This work was financially supported by The Netherlands Center for Multiscale Catalytic Energy Conversion (MCEC), an NWO Gravitation Programme funded by the Ministry of Education, Culture and Science of the government of The Netherlands, and the European Union (ERC, MeltDyn, 101040254). The authors report no conflict of interest.

REFERENCES

- ACRIVOS, A. 1960*a* A theoretical analysis of laminar natural convection heat transfer to non-Newtonian fluids. *AIChE Journal* **6** (4), 584–590.
- ACRIVOS, A. 1960*b* Mass transfer in laminar-boundary-layer flows with finite interfacial velocities. *AIChE Journal* **6** (3), 410–414.
- BEJAN, A. 1993 *Heat transfer*. J. Wiley.
- CARBAJAL VALDEZ, R., JIMÉNEZ PÉREZ, J. L., CRUZ-OREA, A. & MARTÍN-MARTÍNEZ, E. SAN 2006 Thermal diffusivity measurements in edible oils using transient thermal lens. *Int. J. Thermophys.* **27** (6), 1890–1897.
- CENEDESE, C. & STRANEO, F. 2023 Icebergs melting. *Annu. Rev. Fluid Mech.* **55**, 377–402.
- COHEN, C., BERHANU, M., DERR, J. & COURRECH DU PONT, S. 2020 Buoyancy-driven dissolution of inclined blocks: erosion rate and pattern formation. *Phys. Rev. Fluids* **5** (5), 53802.
- COHEN, C., BERHANU, M., DERR, J. & COURRECH DU PONT, S. 2016 Erosion patterns on dissolving and melting bodies. *Phys. Rev. Fluids* **1** (5), 3–5.
- DAVIES WYKES, M.S., HUANG, J.M., HAJJAR, G.A. & RISTROPH, L. 2018 Self-sculpting of a dissolvable body due to gravitational convection. *Phys. Rev. Fluids* **3** (4), 1–18.
- DHAIDAN, N.S. & KHODADADI, J.M. 2015 Melting and convection of phase change materials in different shape containers: A review. *Renew. Sustain. Energy Rev.* **43**, 449–477.
- EASYSOURCE.COM 2005 Latent Heat Table .
- FELTHAM, D. L. 2008 Sea ice rheology. *Annu. Rev. Fluid Mech.* **40**, 91–112.
- GUDHEIM, A.R. 1944 The specific and latent heats of fusion of some vegetable fats and oils. *Oil and Soap* **21** (5), 129–133.
- GUÉRIN, A., DERR, J., COURRECH DU PONT, S. & BERHANU, M. 2020 Streamwise Dissolution Patterns Created by a Flowing Water Film. *Phys. Rev. Lett.* **125** (19), 1–6.
- HOLLAND, M.M., BITZ, C.M. & TREMBLAY, B. 2006 Future abrupt reductions in the summer Arctic sea ice. *Geophys. Res. Lett.* **33** (23).
- HUANG, J.M., TONG, J., SHELLEY, M. & RISTROPH, L. 2020 Ultra-sharp pinnacles sculpted by natural convective dissolution. *Proc. Natl. Acad. Sci. U.S.A.* **117** (38), 23339–23344.
- INCROPERA, F.P. & WITT, D.P. 1990 Fundamentals of heat and mass transfer, third edition. *New York* .
- MERK, H.J. & PRINS, J.A. 1954 Thermal convection in laminar boundary layers III. *Appl. Sci. Res., Sec. A* **4**, 207–221.
- OSTRACH, S. 1953 An analysis of laminar free-convection flow and heat transfer about a flat plate parallel to the direction of the generating body force. *Tech. Rep.*.
- PEGLER, S.S. & DAVIES WYKES, M.S. 2020 Shaping of melting and dissolving solids under natural convection. *J. Fluid Mech.* **900**, A35.
- RISTROPH, L., MOORE, M.N.J., CHILDRESS, S., SHELLEY, M.J. & ZHANG, J. 2012 Sculpting of an erodible body by flowing water. *Proc. Natl. Acad. Sci. U.S.A.* **109** (48), 19606–19609.
- SHI, X.D., BRENNER, M.P. & NAGEL, S.R. 1994 A cascade of structure in a drop falling from a faucet. *Science* **265** (5169), 219–222.
- TURGUT, A., TAVMAN, I. & TAVMAN, S. 2009 Measurement of Thermal Conductivity of Edible Oils Using Transient Hot Wire Method. *Int. J. Food Prop.* **12** (4), 741–747.
- WAGNER, C. 1949 The Dissolution Rate of Sodium Chloride with Diffusion and Natural Convection as Rate-Determining Factors. *J. Phys. Chem.* **53** (7), 1030–1033.
- WELLS, A.J. & WORSTER, M.G. 2011 Melting and dissolving of a vertical solid surface with laminar compositional convection. *J. Fluid Mech.* **687** (2011), 118–140.
- YANG, R., HOWLAND, C.J., LIU, H.-R., VERZICCO, R. & LOHSE, D. 2023*a* Ice melting in salty water: layering and non-monotonic dependence on the mean salinity. *J. Fluid Mech.* **969**, R2.
- YANG, R., HOWLAND, C.J., LIU, H.-R., VERZICCO, R. & LOHSE, D. 2023*b* Morphology evolution of a melting solid layer above its melt heated from below. *J. Fluid Mech.* **956**, 23.

Appendix A. Effect of finite h on T^*

Consider a piece of material of length h , and temperature T_o , lying between $x = 0$ and $x = h$. This is at time $t = 0$ brought into contact with a semi-infinite piece of the same material, between $x = h$ and $x = \infty$, and at temperature T_∞ . The side of the first piece at $x = 0$ is kept at T_o at all times. We are interested in the temperature at $x = h$. With α as defined in the text, the heat equation in both pieces is

$$\frac{\partial T}{\partial t} = \alpha \frac{\partial^2 T}{\partial x^2}. \quad (\text{A } 1)$$

Applying a Laplace transform $L(t) = \int_0^\infty T e^{-st} dt$, taking into account the above mentioned boundary and initial conditions gives for the solution of the Laplace transform of the temperature at $x = h$:

$$L(T(x = h)) = \frac{T_\infty - T_o}{2} \frac{e^{-2h\sqrt{\frac{s}{\alpha}}}}{s}. \quad (\text{A } 2)$$

Using a table of inverse Laplace transforms results for the temperature at $x = h$ in

$$T^* = T_o + \frac{T_\infty - T_o}{2} \operatorname{erf} \left(\frac{h}{\sqrt{\alpha t}} \right). \quad (\text{A } 3)$$